

1 7419

2 A new approach for the vitrification of municipal solid waste
3 incinerator bottom ash by microwave irradiation

4

5 Georgia Flesoura^{1,*}, Nicole Dilissen¹, Georgios Dimitrakis², Jef Vleugels¹, Yiannis Pontikes¹

6 ¹ KU Leuven, Department of Materials Engineering, Kasteelpark Arenberg 44, 3001 Heverlee,
7 Belgium.

8 ² Department of Chemical and Environmental Engineering, Faculty of Engineering, University of
9 Nottingham, Nottingham NG27 2RD, UK.

10 * georgia.flesoura@kuleuven.be

11 nicole.dilissen@kuleuven.be (Nicole Dilissen)

12 Georgios.Dimitrakis@nottingham.ac.uk (Georgios Dimitrakis)

13 jozef.vleugels@kuleuven.be (Jef Vleugels)

14 yiannis.pontikes@kuleuven.be (Yiannis Pontikes)

15

16 **Keywords:** Microwave processing; MSWI bottom ash; Microwave heating; Waste treatment

17

18 **Abstract**

19

20 Encouraging the transition to a circular economy, the valorization of municipal solid waste incinerator
21 (MSWI) bottom ash (BA) has received considerable attention in many processes. In the present work,
22 flash microwave vitrification was effectively realized in a single mode cavity operating at 2.45 GHz
23 within 1.5 min. The closed-loop process was evaluated in terms of energy and power input, treatment
24 time and vitrified bottom ash (VBA) yield rate. The required minimum energy consumption was ~3300
25 kJ/kg. By conducting thermo-electromagnetic multiphysics simulations, the heating mechanism of BA
26 by microwave irradiation was underpinned. This relied on the generation of microwave-induced hot
27 spots inside the material and high power density, in the order of 3×10^7 W/m³, that triggered the onset

28 of BA melting at high heating rates. The inherent cold environment of the microwave cavity, due to the
29 absence of any insulation material, in conjunction with the high silica content of BA promoted the glass
30 forming ability of the melt. This allowed a natural fast cooling of the melt and VBA production,
31 avoiding the cost and environmental impact accompanying conventional quenching. Preliminary
32 characterization of the highly amorphous VBA product was performed and its exothermal heat flow
33 after alkali activation revealed the potential incorporation in the binder of novel building materials.

34 35 **1. Introduction** 36

37 Driven by the approach in Europe that promotes resource recovery and environmental impact reduction,
38 progress has been made on establishing alternative ways of treating waste (European Commission-
39 Environment, 2019). In the framework of the circular economy policy, based on ‘closing the loop’ by
40 utilizing waste for appropriate applications and waste management hierarchy, incineration has been
41 adopted as an attractive waste management technique (European Commission-Environment, 2019.).
42 Through the incineration of municipal solid waste, the volume and mass of waste can significantly be
43 reduced up to 80% (Wei et al., 2011). At the same time, heat is generated, recovered and converted into
44 energy. However, this is not a complete win-win strategy since it leads to the formation of residues in
45 the incineration plant (Sloot et al., 2001), predominantly municipal solid waste incinerator (MSWI)
46 bottom ash (BA).

47 For the purpose of waste valorisation, a straightforward route is the utilization of BA in building
48 materials. Nowadays, BA is used as embankment filler, landfill structure, road sub-base material and
49 aggregate in concrete (Blasenbauer et al., 2020), although the presence of heavy metals confines its use
50 in further applications. Thus, prior to recycling, the MSWI ash requires beneficiation, the
51 implementation of which depends on the ash properties and the aimed application (Joseph et al., 2018).
52 The techniques being already implemented on industrial scale are metal extraction, washing and ageing.
53 Vitrification has attracted attention as the most efficient technique for heavy metals immobilization.
54 Industrializing of the vitrification technology is however considered to be an unaffordable route,

55 because it requires a high temperature operation resulting subsequently in a high energy consumption
56 (Joseph et al., 2018).

57 The European Union's current policy demands for green industrial process technologies (European
58 Parliament and Council, 2018) pledge the use of a sustainable form of energy. In response to this,
59 microwave heating comes to the foreground. This has already received considerable attention for waste
60 stabilization, mainly in the field of radioactive waste (Yuan et al., 2017; Zhang et al., 2016). Microwave
61 heating realises essential benefits over conventional heating methods. In essence, microwave heating is
62 volumetric and is associated with high heating rates that cannot be realised by conventional means. As
63 a result, microwave heating can overcome the heat transfer limitations typically associated with
64 processes operating at high temperatures. In addition, electromagnetic waves can interact selectively
65 with the microwave absorber compounds, depending on the material composition and concomitant
66 dielectric properties. Overall, the volumetric and selective mechanism of microwave heating along with
67 the associated high heating rates, typically result in short treatment times and potentially in significant
68 processing benefits compared to conventional thermal treatments (Ferrera-Lorenzo et al., 2014;
69 Menéndez et al., 2010; Xin-Hui et al., 2011).

70 The synergy between volumetric and selective heating is mainly the case for heterogeneous materials,
71 such as waste and BA, which contain a mixture of compounds that respond differently in an
72 electromagnetic field. Mineral phases with a high dielectric loss factor (e.g. iron oxides (Hotta et al.,
73 2010)) are more susceptible to microwave energy absorption than those with a low loss factor (e.g.
74 quartz, diopside, akermanite, etc. (Rosenholtz and Smith, 1936)), and are thus selectively heated. This
75 was clearly demonstrated in a previous study assessing the dielectric properties of BA subjected to
76 microwave irradiation (Flesoura et al., 2019a). Although BA was found to be a poor microwave
77 absorber at room temperature, the char, produced by the pyrolysis of organic matter, in combination
78 with existing and newly during microwave heating created microwave-absorbing phases like magnetite,
79 metallic iron and aluminum resulted in localized hot spots and high heating rates (Flesoura et al., 2019a).
80 Apart from the material's dielectric properties, the input power density is another parameter affecting
81 the heating mechanism and the overall process. The absorbed or dissipated power, P_d , is directly related
82 to the dielectric loss factor and the local electric field intensity, as given by: (Robinson et al., 2012)

83 $P_d = 2\pi f \epsilon_0 \epsilon'' |E|^2$ (1)

84 where f is the microwave frequency (Hz), ϵ_0 is the permittivity of free space (8.853×10^{-12} F/m), ϵ'' is
85 the dielectric loss factor of a specific mineral phase or material and E is the electric field strength within
86 the material volume (V/m). The electric field strength is determined by the design of the microwave
87 applicator and the applied microwave power. Typically, microwave applicators exist in a single mode
88 or multimode configuration. Single mode microwave applicators produce a single electromagnetic
89 resonance wave, resulting in a high local power density, while multimode applicators produce multiple
90 resonance waves and are associated with lower power densities.

91 To overcome the challenge of the poor microwave absorption of BA at room temperature and establish
92 a controlled heating process, a high electric field intensity, single-mode microwave cavity was used in
93 the current study. To the best of our knowledge, there are no literature reports on the development of a
94 direct microwave BA vitrification process.

95 The aim of this work was to assess the feasibility of using microwave radiation to vitrify BA and define
96 the extent to which it can be attained. Additionally, the underlying heating mechanism of BA was
97 investigated based on a microwave process parametric study in combination with thermo-
98 electromagnetic multiphysics simulations. The potential to alkali-activate the VBA was also assessed.

99

100 **2. Materials and methods**

101 **2.1 Material preparation and characterization**

102 MSWI BA material was provided by Heros Sluiskil BV (The Netherlands). After in-plant quenching
103 (fast cooling) in water and removal of ferrous and non-ferrous metals, the BA was piled up under
104 atmospheric conditions for 2-3 months for stabilization purposes. As-received 0.1-100 mm MSWI BA
105 was dried in a laboratory oven at 105°C until no further change of weight could be recorded. The
106 material was crushed in a disk mill (Retsch DM200), followed by milling in a ring mill (Retsch RS200)
107 to a particle size $< 100 \mu\text{m}$ (Flesoura et al., 2019a).

108 Nitrogen gas pycnometry (Quantachrome, MVP-6DC) was used to determine the real density of the BA
109 and VBA powders. The chemical composition of BA and VBA was determined by wavelength

110 dispersive X-ray fluorescence (Bruker S8). The mineral composition of BA, VBA and sintered BA
111 (SBA) powders was measured by X-ray diffraction (D2 Phaser Bruker). The amorphous phase content
112 was determined by adding 10 wt% of analytical-grade crystalline ZnO to the BA, VBA and SBA as an
113 internal standard. BA, VBA and SBA powder samples were then milled in a McCrone micronizing mill
114 for 7.5 min in ethanol (purity 99.9%) with a corundum grinding medium to assure an appropriate
115 fineness for analysis. X-ray diffraction patterns were recorded at room temperature in the 2θ range from
116 10° to 70° , using Cu K_α radiation at an acceleration voltage of 45 kV, a current of 30 mA, a step size of
117 0.020° and a counting time of 2.5 s per step. Qualitative analysis was performed using EVA V.3.1
118 (Bruker AXS) and quantitative analysis using Topas-Academic V.5 (Coelho, 2016), through the
119 Rietveld method. Structural data were taken from the ICSD database.

120 Considering VBA valorization in alkali activated materials, an evaluation of the reactivity of VBA in
121 terms of heat release, was performed through isothermal calorimetry. A milled VBA sample was
122 prepared by mixing 3 g of the glass with the activator in ampoules with a Heidolph RZR 2041 mixer at
123 approximately 2500 rpm for 90 seconds. As a sodium silicate activator, a $\text{SiO}_2/\text{Na}_2\text{O}$ ratio of 1.6 and
124 $\text{H}_2\text{O}/\text{Na}_2\text{O}$ ratio of 20 was used. The solution/glass powder mass ratio was 0.4. The heat flow of the
125 sample was measured for 7 days at a constant temperature of 20°C .

126 To evaluate the efficiency of vitrification on the leachability of heavy metals from the VBA, leaching
127 test was performed on the VBA and raw BA sample according to EN 12457-4 [19]. The leached heavy
128 metal content was measured by inductively coupled plasma mass spectroscopy (ICP-MS, Agilent 7500
129 cx) and ion chromatography (IC, Dionex ICS 2000).

130

131

132 **2.2 Microwave processing in a single mode cavity**

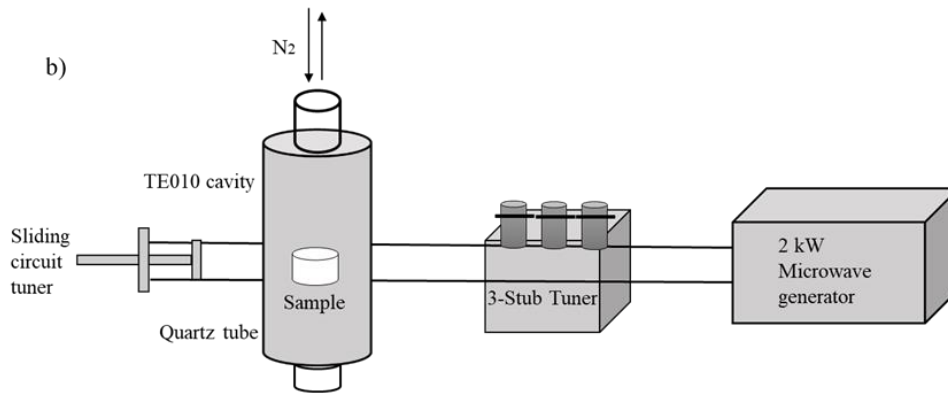
133 Direct microwave vitrification of BA was performed in a 2450 ± 25 MHz frequency single mode
134 microwave setup. Fig. 1 shows an image of the microwave system used for the experiments, along with
135 a schematic of the constituent components. The system is composed of a microwave generator with a
136 power output of 0-2 kW connected to a TE_{010} cavity (SAIREM, France) via a WR430 waveguide.

137 Impedance matching between sample and microwave source, in order to maximize the amount of
138 absorbed incident power, was performed using a 3-stub and a sliding short circuit. 30 g of loose MSWI
139 BA powder was placed in a quartz tube (30 mm height and 40 mm diameter), positioned along the
140 vertical axis of the cylindrical cavity at the maximum electric field strength. The top of the tube was
141 connected to an off-gas collection system. A 5 ml/min nitrogen flow was introduced from the top of the
142 tube in order to ensure an inert atmosphere and reducing conditions. Prior to the experiments, the sliding
143 short circuit was positioned to minimize the reflected power and fixed for all the experiments. Only
144 small adjustments of the 3-stub tuners were performed during the experiments, while both the incident
145 and reflected power were recorded in real time using Agilent power sensors and HomSoft software for
146 energy data logging. The four open viewpoints of the cavity enabled temperature measurements using
147 pyrometers to measure the surface temperature and to detect potential temperature gradients. A single-
148 color optris pyrometer (CT LT20, temperature range between 50 °C and 975 °C) was used to measure
149 the temperature on the sample surface, whereas a single-color AMETEK pyrometer (Land, AMETEK,
150 temperature range between 600 °C and 1600 °C) was focused on the hot spots of the sample. Due to the
151 volumetric heating and concomitant temperature gradients inside the material, the temperature profiles
152 are not reported. On the contrary, the temperature distribution throughout the material powder pellet
153 was simulated as explained below.



154

155



156

157 **Figure 1:** Overview (a) and schematic (b) of the microwave system used for BA vitrification. The red
 158 arrow in (a) points out the frontal view inside the cavity, of which a zoomed in version is depicted in
 159 Fig. 7.

160

161 Table 1: MSWI BA microwave treatment experimental matrix

| Energy input | | Experimental parameters | | | Output |
|----------------------------------|-------------------------------|-------------------------|-----------------|----------------------|--|
| Theoretical Energy Input (kJ/kg) | Specific Energy Input (kJ/kg) | Reflected Power (W) | Power Input (W) | Treatment time (min) | VBA yield (%) ($m_{\text{bead}} * (100/m_{\text{BA}})$) |
| 2400 | 783 | 159 | 200 | 6 | 0±0 |
| 2400 | 1501 | 121 | 400 | 3 | 0±0 |
| 2400 | 1276 | 199 | 600 | 2 | 0±0 |
| 2400 | 1087 | 309 | 800 | 1.5 | 4±0 |
| 4800 | 3405 | 60 | 200 | 12 | 38±7 |
| 4800 | 3373 | 67 | 400 | 6 | 51±3 |
| 4800 | 4144 | 56 | 600 | 4 | 43±2 |
| 4800 | 3268 | 49 | 800 | 3 | 65±4 |
| 9600 | 8269 | 24 | 200 | 24 | 64±2 |
| 9600 | 7998 | 38 | 400 | 12 | 69±3 |
| 9600 | 8944 | 24 | 600 | 8 | 80±0 |
| 9600 | 8578 | 35 | 800 | 6 | 86±0 |
| 14400 | 12851 | 18 | 200 | 36 | 52±0 |
| 14400 | 12415 | 38 | 400 | 18 | 66±0 |
| 14400 | 12802 | 32 | 600 | 12 | 82±2 |

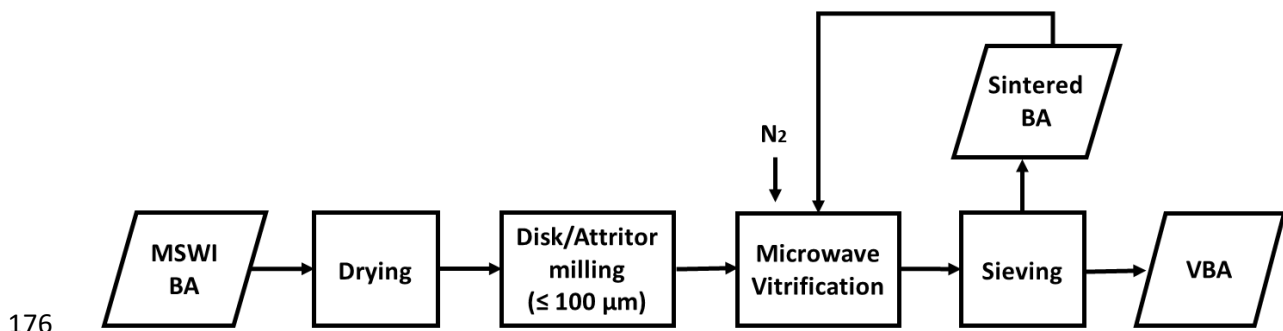
162

163 The effect of the electromagnetic power input and exposure time on the MSWI BA to vitrified bottom
 164 ash (VBA) conversion yield (presented in the Results and Discussion paragraph), was systematically
 165 studied (Table 1). 30 g MSWI BA powder was used for the microwave vitrification process under an

166 applied power ranging from 200 to 800 W and for 1.5 to 36 minutes. Increasing the power level above
 167 800 W resulted in plasma formation and a concomitantly high reflected power. Hence, the power level
 168 of 800 W was not applied for more than 6 min. In order to assess the consistency and repeatability of
 169 the results, each experiment was duplicated and the reported results are the average values. The specific
 170 energy input (kJ/kg), which is equivalent to the specific energy consumption was calculated as:

171
$$\text{Specific Energy Input (kJ/kg)} = \frac{P \text{ (kW)} * t \text{ (s)}}{m \text{ (kg)}} \quad (2)$$

172 with P (kW), the effectively absorbed power (or power consumption), which was calculated by
 173 subtracting the recorded reflected power from the input power, t (s), the treatment time and m (kg), the
 174 sample mass. Four experimental parameter combinations with the same theoretical energy input were
 175 assessed.



177 **Figure 2:** Flowchart of the BA microwave vitrification process.

178
 179 The flowchart of the microwave vitrification process followed in this study is presented in Fig. 2. The
 180 microwave heat treatment resulted in two products, including VBA, in the form of a flattened fully
 181 dense glass bead, and surrounding loose SBA powder. At the end of each experiment, manual sieving
 182 was performed to separate the VBA bead from the SBA powder. The mass of the produced glass bead
 183 was measured and converted into a yield (%) following the equation, $(m_{\text{bead}} * (100/m_{\text{BA}}))$, where m_{bead}
 184 was the weight of the glass bead and m_{BA} was the initial weight of BA (equal to 30 g for all the
 185 experiments). The weight losses arising during heating BA, due to loss of water and -OH, dissociation
 186 of carbonates, Fe^{3+} reduction, etc., were not taken into account; the exact temperature of the sample
 187 could not be assessed with precision thus results would introduce an error. Hence, the actual VBA yield

188 is higher than the reported values. Of note is that the formation of VBA is directly related to the position
189 of the maximum E-field in the cavity, the power input, the treatment time and the thermal losses.

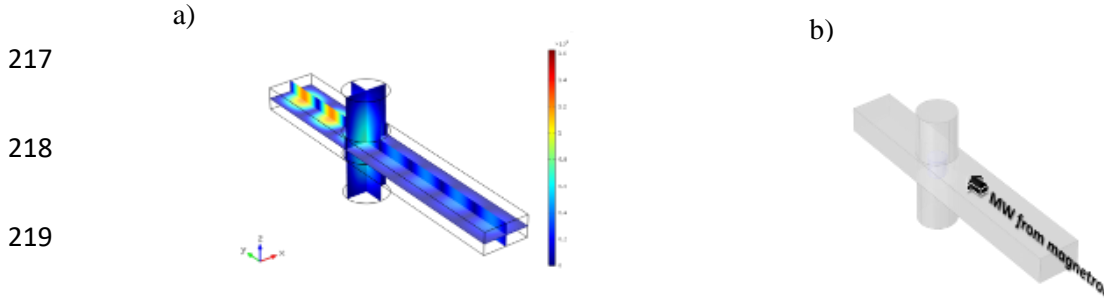
190

191 **2.3 Electromagnetic field and temperature simulations**

192 The experimental parameters that resulted in the highest vitrification output (VBA yield) were used to
193 simulate the temperature distribution in the powder compact using multiphysics COMSOL simulations,
194 combining microwaves and heat transfer. This concerns the 86% of VBA yield at 800 W power input
195 and 6 min treatment time (Table 1). The quartz tube, classified as a transparent material for microwaves,
196 was not considered for the simulations. The electric field strength distribution inside the waveguide and
197 the cavity, in the absence of a BA sample, is presented in Fig. 3a. The quartz tube filled with BA powder
198 was positioned in the centre of the cavity, where the electric field strength was maximum (Fig. 3a). The
199 dimensional parameters were defined for waveguide, cavity, quartz tube and the BA sample, placed in
200 the center of the cavity, in 3D (Fig. 3b). The port for microwaves to enter the waveguide was defined
201 at the waveguide boundary (lower right rectangular surface in Fig. 3b). The multiphysics involved were
202 electromagnetic waves in frequency domain (*emw*) and heat transfer in solids (*ht*). In (*emw*), the wave
203 equation, perfect electric conductor and initial values were predefined and kept unchanged, whereas the
204 port had to be defined. The port type was rectangular, wave excitation was on, port power input was set
205 to 800 W, port phase was 0 rad and port mode was TE₁₀. In (*ht*), the heat transfer in solids and initial
206 values were predefined. A convective heat flux with external natural convection by air at ambient
207 pressure (1 atm) and temperature (20 °C) was applied to cavity and waveguide boundaries. Diffuse
208 surface radiation at ambient temperature (20 °C) was applied as boundary condition to the BA surface.
209 The multiphysics software couples the two before-mentioned physics, i.e., the electromagnetic losses
210 cause heating and the heating in turn influences the electromagnetic properties. A physics-controlled
211 mesh with extremely fine element size (the finest element size that exists) was used. Within the BA
212 sample, 9 domain point probes were defined at specific x,y,z coordinates, 6 at the edges (e1 to e6) and
213 3 in the middle (m1 to m3), to track the evolution of the temperature at these specific locations of the

214 BA (Fig. 8c). The study was frequency-transient with a frequency of 2.45 GHz, a time of 6 min and
215 time step of 0.5 min.

216



220

221 **Figure 3:** a) Electric field strength (V/m^3) distribution in the waveguide (horizontal bar) and cavity
222 (vertical cylinder) without BA sample and b) with BA sample (small cylinder inside the cavity
223 configuration as used for the multiphysics simulations. The magnetron is located on the right hand side
224 of the waveguide. X-Y-Z axes are used as reference, to which the results in Figs. 6 and 7 can be
225 correlated.

226

227 Additional parameters used within the multiphysics equations were defined by the materials. The
228 material in the cavity was defined as air, for which the parameters were available in COMSOL in the
229 Built-in Menu. The parameters for the BA sample were provided as input parameters by the user. The
230 relative permittivity, relative permeability and electrical conductivity was used for electromagnetic
231 wave physics, whereas the thermal conductivity, density and heat capacity was necessary for the heat
232 transfer in solids. Surface emissivity was added to the boundary condition of BA. The input data for
233 these parameters are given in Table 2. Relative permittivity and heat capacity depend on temperature,
234 whereas the other parameters were defined as constant. Relative permeability was set to 1, since BA is
235 non-magnetic (Flesoura et al., 2019a). The electrical conductivity was 0.000197 S/m, approximated as
236 that of a slag with similar composition (Woollacott et al., 1975). The thermal conductivity of BA was
237 approximated as that of concrete, basalt, glass and set to 1 W/(m.K). The density was calculated from
238 mass (30 g) and volume within the quartz tube (30 mm height and 40 mm diameter) to be 800 kg/m³.
239 Note that this is a powder in the experiments, whereas this was considered as a bulk solid in the
240 simulation. The surface emissivity was chosen as 0.95.

241 Table 2: BA properties used in the multiphysics simulations. Equations and constant values are
 242 explained in the text.

| Property | Value | Unit | Physics module |
|-------------------------|---------------------------------|-------------------|------------------------|
| Relative permittivity | $\epsilon'(T) - \epsilon''(T)i$ | - | <i>emw</i> |
| Relative permeability | 1 | - | <i>emw</i> |
| Electrical conductivity | 0.000197 | S/m | <i>emw</i> |
| Thermal conductivity | 1 | W/(m.K) | <i>ht</i> |
| Density | 800 | kg/m ³ | <i>ht</i> |
| Heat capacity | $C_p(T)$ | J/(kg.K) | <i>ht</i> |
| Surface emissivity | 0.95 | - | <i>Diffuse surface</i> |

243

244 The temperature-dependent equation for the relative permittivity consists of the dielectric constant $\epsilon'(T)$
 245 and dielectric loss factor $\epsilon''(T)$ (Table 3), that are based on the dielectric measurements from (Flesoura
 246 et al., 2019a). A window type function was used for $\epsilon'(T)$ and $\epsilon''(T)$ with temperature intervals.

247 Table 3: Functions used for the simulations of $\epsilon'(T)$ and $\epsilon''(T)$ with temperature intervals.

248

| T_{Start} (K) | T_{End} (K) | $\epsilon'(T)$ |
|-----------------|---------------|--|
| 314 | 588 | $0.0005 \times T + 2.1659$ |
| 588 | 670 | $0.0138 \times T - 5.4822$ |
| 670 | 1108 | $0.0025 \times T + 2.1568$ |
| 1108 | 1700 | $-3.1818 \cdot 10^{-5} \times T^2 + 0.0831 \times T - 48.38$ |
| T_{Start} (K) | T_{End} (K) | $\epsilon''(T)$ |
| 314 | 573 | $2 \cdot 10^{-7} \times T^2 - 0.0001 \times T + 0.024$ |
| 573 | 670 | $0.0098 \times T - 5.6286$ |
| 670 | 948 | $0.0012 \times T + 0.092$ |
| 948 | 1108 | $0.0086 \times T - 7.0767$ |
| 1108 | 1338 | $0.026 \times T - 26.195$ |

249

250

254 3. Results & Discussion

255 3.1 Assessment of microwave vitrification of MSWI BA

256 The microwave heat treatment resulted in two products, i.e. a fully dense VBA glass bead and
 257 agglomerated and loose SBA powder, as shown in Fig. 4, for the BA heat treated at 400W for 6 minutes.

258 The VBA yield, is summarized in Table 1.



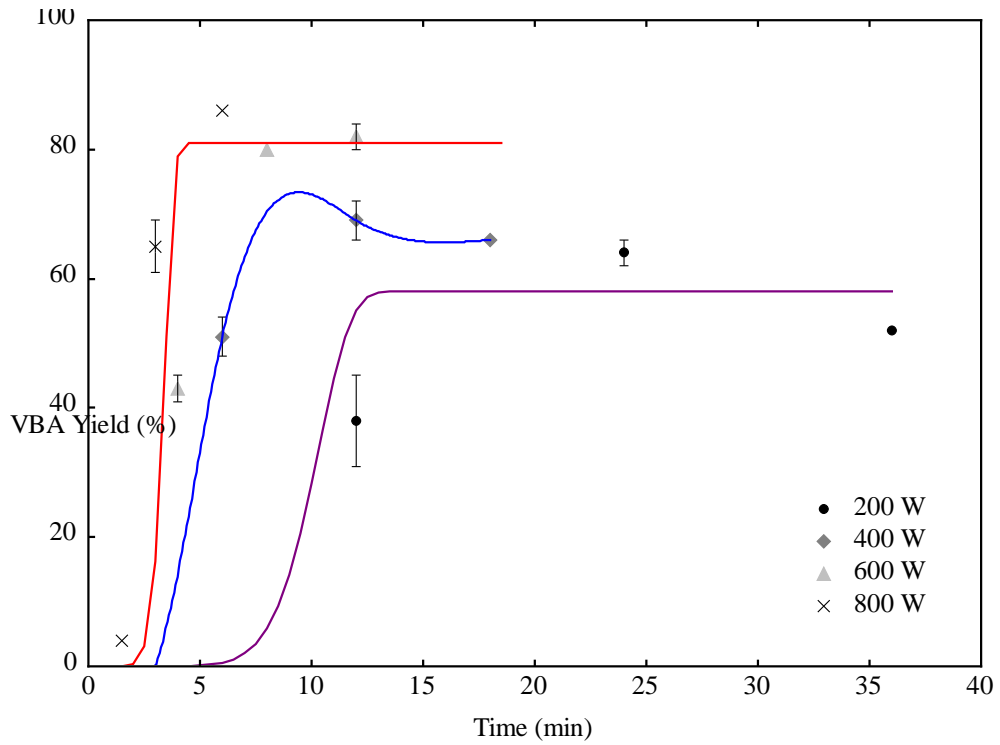
259

260 **Figure 4:** Microwave processed BA products (400W for 6min); (a) VBA bead and SBA powder and
261 (b) VBA glass bead halves after fracturing.

262 The evolution of the glass yield (%) as a function of the heating time at 4 input power levels is presented
263 in Figure 5. The glass yield varied from 0 % to 86 %, depending on the process conditions. It is clear
264 that the yield reaches a saturation level 80% at power inputs of 600 and 800 W. The scatter plots are
265 sigmoidal as a function of time and shift to shorter treatment times at higher input power levels.

266 The intrinsic microwave heating mechanism of BA was revealed by the effect of the calculated specific
267 energy input and power input on the VBA yield and was confirmed by the simulation results, presented
268 in section 3.2. Fig. 6 shows the evolution of the VBA yield as a function of the specific energy input at
269 different levels of applied power input.

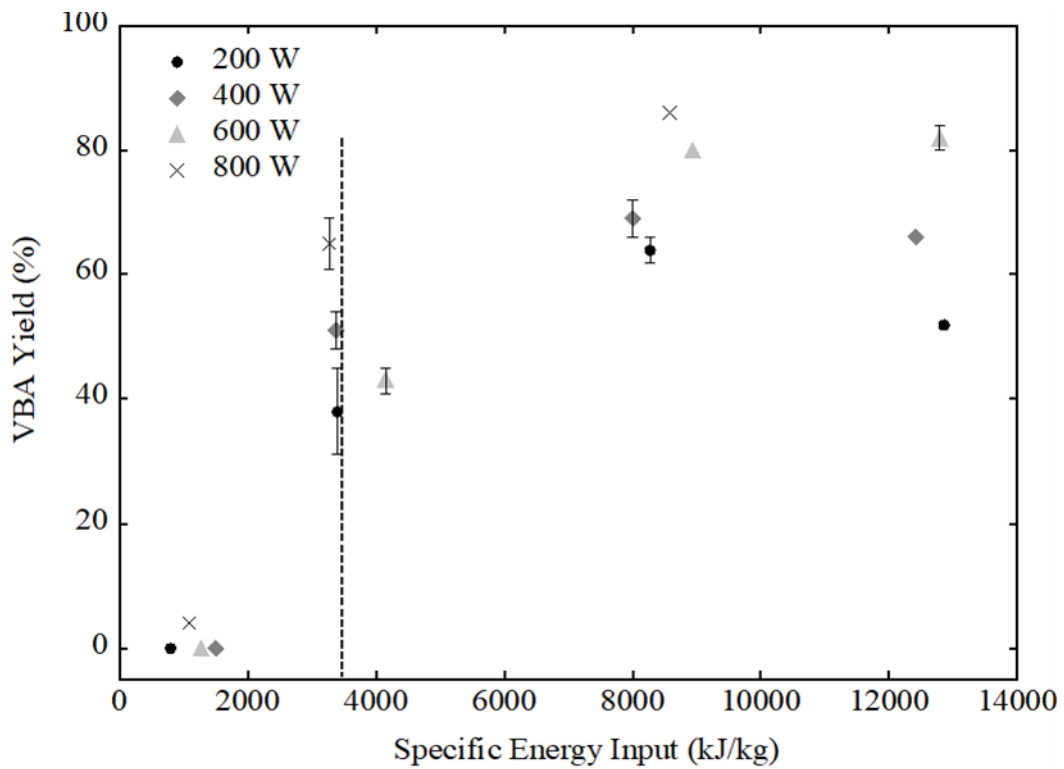
270



271

272 **Figure 5:** Effect of heating time and power level on the glass bead production during microwave
 273 processing of 30 g BA in a single mode cavity.

274



275

276 **Figure 6:** Effect of the specific energy input on the VBA production yield during microwave processing
 277 of 30 g BA samples in a single mode cavity. The dotted line indicates the sigmoidal trend of the scatter
 278 plots, near the value of the threshold energy input.

279 A yield of 63 % was obtained with an energy input of ~3300 kJ/kg. Further increasing the energy input
280 up to ~8600 kJ/kg allowed to increase the VBA yield up to a maximum of 86%, implying that the
281 absence of thermal insulation material around the quartz tube and the surrounding cold inherent
282 environment of the cavity hindered complete vitrification of the complete powder bed due to the axial
283 and radial thermal gradients (as explained in depth in section 3.2). For comparison, an energy
284 consumption of 2600 kJ/kg was reported for MSWI fly ash vitrification by thermal plasma melting
285 (Huang et al., 2014).

286 A threshold energy input of ~3300 kJ/kg, as indicated by the vertical line in Fig. 6, was required to
287 initiate vitrification which was even possible with a power input of only 200 W. The maximum yield
288 however was reached faster when using a higher input power, specifically at 600 W and 800 W, as
289 indicated by the shift of the sigmoidal curves in Fig. 5. On the contrary, BA vitrification did not take
290 place at 200 W, 400 W and 600 W after 6, 3 and 2 min respectively. This clearly indicates the
291 vitrification of VBA is energy density controlled, and conversion goes faster at higher power input,
292 providing the threshold energy level is reached. A higher power input at constant duration also results
293 in a larger volume of the powder compact reaching this threshold, resulting in a higher yield, explaining
294 the slightly higher yields at 800 W power levels.

295 As a remark, there is no linear trend between the total energy input and the VBA yield, as higher energy
296 dissipation did not lead to higher yields (see Fig. 6). Additionally, it is worth highlighting that the same
297 theoretical energy input for different power-time combinations (see Table 1) did not result in the same
298 VBA yield, implying the BA microwave vitrification process was not in thermodynamic equilibrium.
299 Microwave BA vitrification was conversely favored by a high power density, i.e. high applied power
300 levels (e.g for 600 W and 800 W) for shorter times (Fig. 6).

301 A potential reason for the above lies in the non-thermal interactions between BA and microwave
302 irradiation by microplasma generation (Hopwood et al., 2014). As mentioned, BA is a mixture of
303 various mineral phases and organic matter that respond differently when subjected to electromagnetic
304 energy. Localized hot spots, known as microplasmas, are initiated in the char, produced by the pyrolysis
305 of organic matter around 320°C and in iron metallic particles that are formed during the reduction of

306 iron oxides. These randomly located microplasmas were visible in the form of small sparks or hot spots
307 that exhibited a thermal runaway, which lasted only a couple of seconds. Visible evidence of this
308 phenomenon when realizing BA vitrification at 800 W is shown in Fig. 7, which presents in high
309 magnification the quartz tube filled with BA powder, when treated at 800 W for 1.5 min. The
310 photograph was taken from the frontal viewpoint of the cavity, where the arrow in Fig.1 is placed. Such
311 microwave-driven micro-plasmas were reported to exhibit in all carbon materials (Menéndez eal.,
312 2011).



313

314 **Figure 7:** Frontal view inside the cavity, showing the quartz tube filled with BA powder, when treated
315 at 800 W for 1.5 min, evidencing a local hot spot or microplasma (circled area).

316

317 At the microwave induced hot spots, favored also by the lack of oxygen and the inert gas use,
318 vitrification initiated. This potentially explains why the process appears to be benefited more by the
319 magnitude of the applied power rather than the total energy input. The above described phenomenon
320 can be better assessed by taking into account the Eq. (3), indicating that the heating rate ($\Delta T/\Delta t$) is
321 proportional to the power density. Therefore, when the absorbed microwave energy is increased, the
322 power density increases as well, giving rise to higher heating rates (Shang et al., 2006).

323
$$\frac{\Delta T}{\Delta t} = \frac{Pd}{\rho Cp} \quad (3)$$

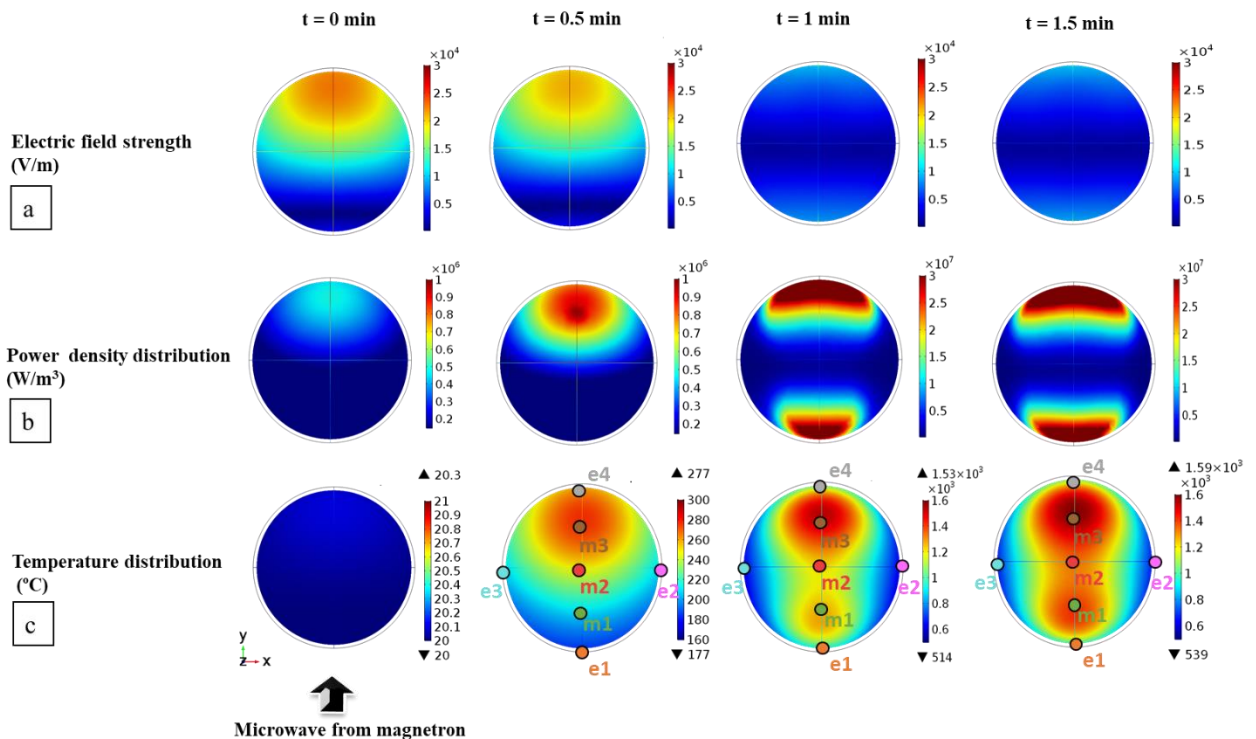
324 with T, the temperature ($^{\circ}\text{C}$), t, the time (s), P_d , the power density (W/m^3), ρ (kg/m^3), the density and
325 C_p ($\text{J}/\text{kg}\cdot\text{K}$), the heat capacity of the material. The inherent difficulty of accurate temperature
326 measurements in microwave configurations required simulations in order to visualize the electric field,
327 power density and the resulting temperature distribution throughout the BA sample (Kappe, 2013).

328 **3.2 Electromagnetic field and temperature distribution simulation**

329 The electromagnetic field along with heat transfer simulations were performed for a 800 W power input.
330 It should be noted that although the simulation results (Fig. 8 and Fig. 9) correspond to an instant time,
331 the electric field and power density distributions change according to the temperature increase and to
332 the associated dielectric properties of BA material. Once the magnetron was switched on and 800 W
333 power was forwarded to the BA powder bed, the dielectric properties instantly changed (Flesoura et al.,
334 2019a) causing a shift of the electric field peak from the center of the cavity (Fig. 3a) to the edge of the
335 sample (Fig. 8a, t=0 min). In addition, the slight increase of the dielectric properties at room temperature
336 (Fig. 8c, t=0 min) only slightly increased the electric field strength from 1.6×10^5 V/m to 2.4×10^4 V/m
337 (Fig. 8a, t=0 min). Similarly, as the power density is proportional to the square of the electric field
338 strength and to the material's loss factor (Eq. 1), it only reached a moderate value of 0.5×10^6 W/m³ at
339 the edge of the BA powder bed (Fig. 8a, t=0 min). Within 0.5 min of constant power input, the highest
340 achieved temperature was found to be equal to almost 300 °C, at the position where the field strength
341 and power density created a hotspot (Fig. 8c, t=0.5 min). This is potentially explained by the substantial
342 effect of the field strength on the absorbed power and temperature distribution, since the dielectric
343 properties of BA were hardly affected in this temperature range. This behavior complied with the slow
344 evolution of the experimentally measured dielectric properties of BA up to 320 °C (Flesoura et al.,
345 2019a). Beyond 0.5 min (30 s), crucial changes governed the evolution of the temperature and power
346 density. As previously reported (Flesoura et al., 2019a), char production around 320 °C promoted the
347 generation of the localized hotspots, due to microplasma formations. These hot spots can be denoted at
348 location m1 and m3 along the y axis (height of the sample) in Fig. 8c, t=1 min, in which the temperature
349 instantly raised to 1530 °C and 1200 °C respectively, inducing the onset of BA melting. Based on
350 FactSage calculations, using the FactPS and FactOxid database, the melting temperature of BA was
351 estimated to be between 1200 °C and 1250 °C. Although the bulk temperature of the BA was higher
352 than the edges (Fig. 8c, t=1 min, points e3 and e2), creating an 'inverse' temperature gradient (Shepherd
353 et al., 2018), the sample was heated volumetrically when t=1 min (Fig. 8c and Fig. 9a). A power density
354 equal to $2\text{-}3 \times 10^7$ W/m³ was sufficient to induce flash BA melting within a few seconds (Fig. 9a and b).
355 Further increase in treatment time (t=1.5 min) did not contribute to a significant temperature rise (see
356 Fig. 9a), as the highest achieved temperature was 1590 °C (Fig. 8c, t=1.5 min, e4 point). The existence

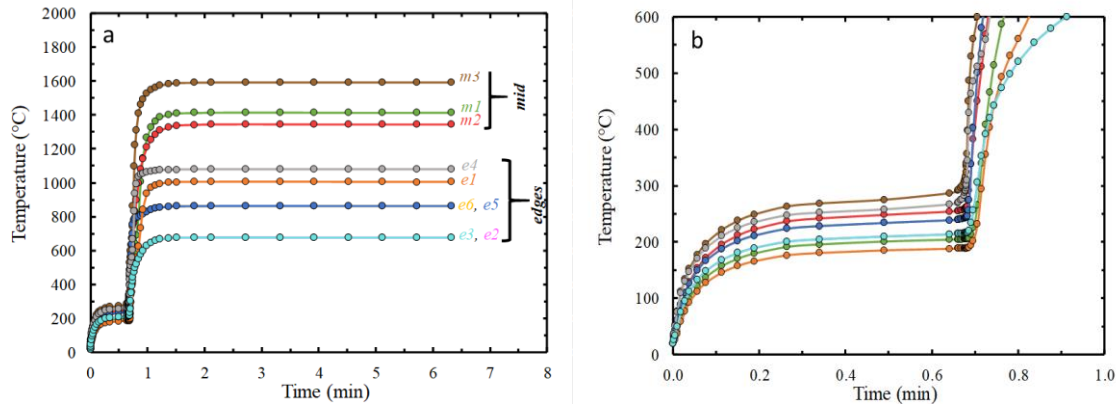
357 of molten BA beyond 1 and 1.5 min, as predicted by the simulation results, was proven by the
 358 experiment performed at 800 W power input for 1.5 min which delivered a 4 wt% VBA yield.
 359 According to Fig. 9b, thermal equilibrium was achieved in the system beyond 1.5 min, implying an
 360 equal amount of absorbed energy and loss to the cold surrounding environment by radiation and
 361 convection. The longer dwell time however resulted in an increased conversion, i.e. growth of the
 362 viscous glass bead, with a total yield of 86 wt% after 6 minutes (Table 1). The natural quenching (fast
 363 cooling) in the thermal insulation-free microwave cavity was fast enough to avoid glass forming during
 364 cooling.

365



366

367 **Figure 8:** Simulated electric field strength (a), power density distribution (b) and temperature
 368 distribution (c) during microwave vitrification of BA at 800 W after 0 min, 0.5 min, 1 min and 1.5 min
 369 processing time.



370

371 **Figure 9:** Simulated heating profile during microwave vitrification of BA at 800 W (a) during the
 372 first 6 min and (b) the first minute and the first The e1-e6 and m1-m3 locations are marked in Fig.
 373 8(c).

374

375 3.3 Characterization of the microwave MSWI BA products

376 3.3.1 Characterization of microwave produced VBA

377 The chemical composition of the BA starting material and the average composition of the VBA
 378 produced under the different process conditions summarised in Table1, which is close to the overall BA
 379 composition, is presented in Table 4. VBA is mainly composed of SiO₂, CaO, Fe₂O₃, Al₂O₃ and MgO
 380 (expressed as oxides).

381 Table 4: Chemical composition of the raw BA starting powder and microwave VBA in wt%, as
 382 measured by WDS-XRF (estimated relative error is 10 %; expressed as oxides), the amount of
 383 amorphous phase in wt%, and density in g/cm³. The VBA composition is the average composition of
 384 the VBA beads obtained from the experiments described in Table 1 (basically 12 beads and their
 385 duplicates).

| | SiO ₂ (wt%) | CaO (wt%) | Fe ₂ O ₃ (wt%) | Al ₂ O ₃ (wt%) | MgO (wt%) | Na ₂ O (wt%) | Other (wt%) | Amorphous fraction (wt%) | Density (g/cm ³) | LOI |
|----------------|---------------------------|-----------------|---|---|----------------|----------------------------|----------------|-----------------------------|---------------------------------|-----|
| Raw BA | 47.80 | 18.30 | 10.00 | 9.39 | 2.04 | 4.08 | 8.39 | 69.2 | 2.6 | 7.5 |
| Average VBA | 49.63 ± 0.02 | 20.24 ± 0.01 | 11.26 ± 0.01 | 9.92 ± 0.03 | 2.47 ± 0.00 | 0.93 ± 0.02 | 5.55 ± 0.01 | 90.0 ± 4.3 | 2.7 ± 0.01 | 0.2 |

386

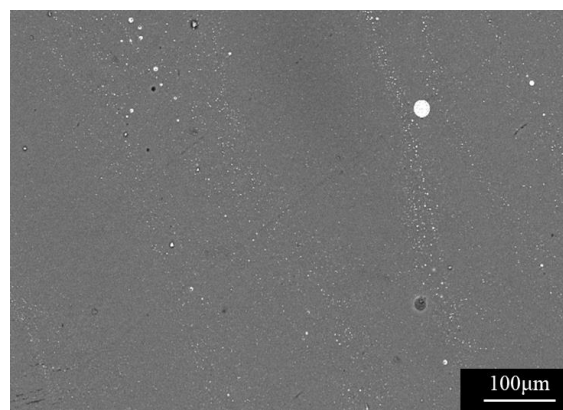
387 The average mineralogical composition of the microwave VBA produced under different process
 388 conditions is presented in Table 5. The crystalline phases embedded in the glass matrix are mainly
 389 anorthite, corundum, clinopyroxene, gehlenite quartz, wollastonite and metallic iron. All VBA
 390 products presented a high amorphous content, varying from 82 wt% to 95.4 wt%. The VBA products
 391 formed at 200 W had the lowest amorphous content, between 82 wt% and 84.8 wt%, whereas the

392 VBA products made at 600 W and 800 W had the highest glass content (between 91 wt% and 95.4
 393 wt%). All VBA materials demonstrated an increased glass content compared to the starting BA
 394 powder (Table 4), which is associated with the high glass forming ability of the BA starting powder
 395 in the presence of a silicate network. The high silica content results in a melt with high viscosity and
 396 configurational entropy that shows increased resistance to nucleation and crystallisation and therefore
 397 produces a glassy material as experimentally confirmed (Mysen and Richet, 2005).

398 Table 5: Average mineralogical composition of the microwave VBA in wt%, as measured by XRD and
 399 quantified by Topas (estimated relative error: 10 %) and mineralogical composition of the microwave
 400 VBA-600-8, VBA-800-6 and VBA-600-12 samples as the ones with yield over 80 %. The VBA
 401 composition is the average composition of the VBA beads obtained from the experiments described in
 402 Table 1 (basically 12 beads and their duplicates) and the composition of the VBA-600-8, VBA-800-6
 403 and VBA-600-12 is the average of the duplicates.

| | Amorphous | Anorthite | Corundum | Clinopyroxene | Gehlenite | Iron | Quartz | Wollastonite |
|-------------|-----------|-----------|----------|---------------|-----------|---------|---------|--------------|
| Average VBA | 90.0±4.3 | 1.1±0.6 | 1.2±0.5 | 2.8±1.9 | 1.0±0.6 | 1.1±0.6 | 0.4±0.2 | 2.1±0.8 |
| VBA-600-8 | 93.0±0.0 | 0.5±0.1 | 0.9±0.2 | 2.8±0.3 | 1.0±0.1 | 0.9±0.1 | 0.2±0.1 | 0.7±0.2 |
| VBA-800-6 | 94.3±0.2 | 0.5±0.3 | 0.4±0.1 | 1.7±0.2 | 0.4±0.1 | 1.3±0.2 | 0.6±0.1 | 0.6±0.2 |
| VBA-600-12 | 90.8±0.1 | 1.2±0.2 | 2.1±0.2 | 3.1±0.3 | 0.4±0.1 | 1.2±0.1 | 0.4±0.1 | 1.5±0.2 |

404



405

406 **Figure 10:** EPMA-BSE image of the amorphous region of the VBA-800-6 material.

407

408 Table 6: EPMA-WDX compositional analysis of the amorphous phase in wt% (\pm standard deviation).
409 At least 10 points were measured for the analysis.

| | SiO ₂ | CaO | Fe | Al ₂ O ₃ | MgO | Na ₂ O |
|-----------|------------------|----------------|---------------|--------------------------------|---------------|-------------------|
| VBA-800-6 | 54.9 \pm 0.5 | 17.8 \pm 0.2 | 4.5 \pm 1.8 | 8.8 \pm 0.2 | 1.3 \pm 0.3 | 1.9 \pm 0.4 |

410

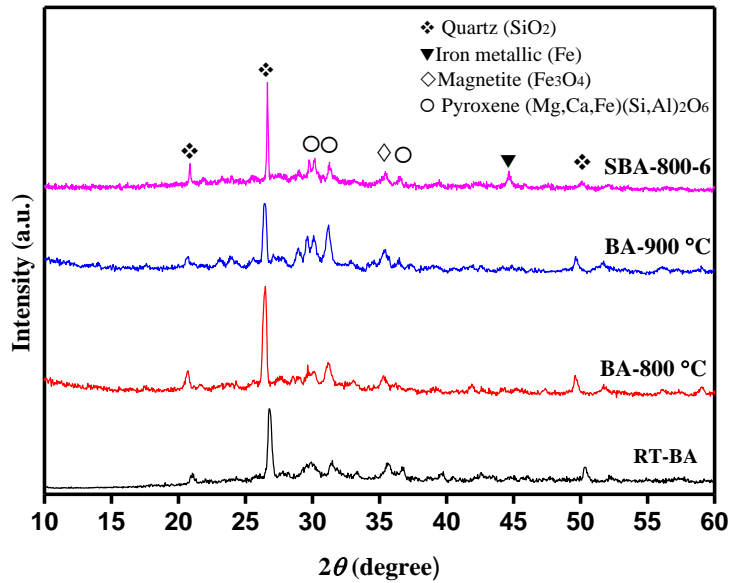
411 Microstructural analysis was performed on the VBA produced at 800 W for 6 min (VBA-800-6). This
412 material was chosen because of the high glass yield (86 wt%) and the increased amorphous content (94
413 wt%). The EPMA image, presented in Figure 10, suggests a homogeneous glassy phase, absence of
414 crystals, with dispersed iron metallic particles presented as the white dispersed phase. The formation of
415 a calcium aluminosilicate (Ca-Al-Si) glassy matrix with dispersed iron (Fe), which has been presented
416 in Tables 4 and 5, is also confirmed by the micro-chemical analysis employed on the amorphous phase.
417 Table 6 reports the average composition of at least 10 point analyses on the amorphous region.

418

419 **3.3.2 Characterization of microwave produced sintered BA**

420 SBA, i.e. the remaining BA powder without the VBA glass bead (part 3, Fig.11), could be recirculated
421 in the microwave vitrification process (Fig. 2) to be vitrified. As a proof of concept, the sintered BA
422 powder, 30 g of residual BA coming from the experiments performed at 800 W for 6 min, was used for
423 microwave vitrification.

424 Aiming to estimate the temperature at which the sintered BA powder has been formed, the XRD pattern
425 was compared with those of HTXRD measurements recorded under reducing atmosphere, reported
426 elsewhere (Flesoura et al., 2019a). The formation of Fe₃O₄ and Fe⁰ (Fig. 11) indicates that the reached
427 temperature of the SBA powder (SBA-800-6) was in the 800-900 °C range, being also in accordance
428 with the simulated temperature for point e3 and e2 presented in Fig 8c, t=1.5 min. The mineral phases
429 that have been formed in the SBA powder (mainly Fe₃O₄, FeO and Fe⁰) have been reported to be more
430 prone to microwave energy absorption than the ones present in BA (Flesoura et al., 2019a). The iron
431 oxides in SBA allowed the almost complete (86 wt%) vitrification of the sintered BA within 3 min,
432 instead of 6 min. The decreased processing time contributed to a lower energy consumption, equivalent
433 to 3438 kJ/kg.

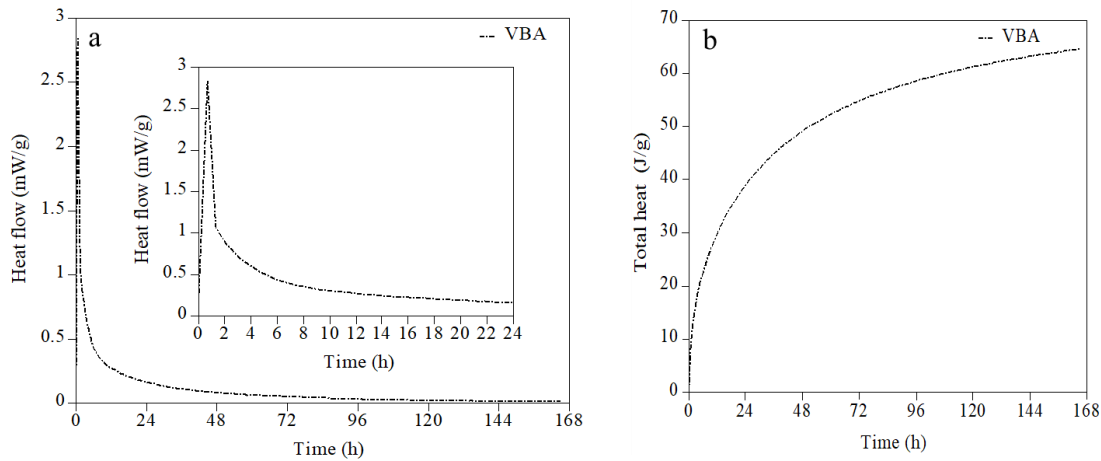


435

436 **Figure 11:** XRD patterns of BA at room temperature (RT-BA), SBA-800-6, and BA at 800°C and
 437 900°C (Flesoura et al., 2019a).

438 Exploring valorization routes for the produced VBA, the potential to be used as a precursor for the
 439 synthesis of alkali activated materials, e.g. inorganic polymers, was assessed through isothermal
 440 calorimetry measurements. Figure 12 shows the heat flow of an alkali activated mixture of VBA-800-
 441 6 (produced as described in section 3.3.2). One exothermic peak is observed immediately after mixing
 442 VBA with the activating solution. This peak could be assigned to wetting (Onisei et al., 2015) and
 443 dissolution reactions. Fast kinetics have also been observed in other silica-rich glasses with similar
 444 chemical composition that can be considered as reference materials. Alkali activating microsilica and
 445 rice husk ash (Gao et al., 2017), ground granulated blast furnace slag with fly ash mixtures (Alonso and
 446 Palomo, 2001; Kumar et al., 2010; Luukkonen et al., 2018) and synthetic VBA (Flesoura et al., 2019b)
 447 also generated a wetting and dissolution exothermic peak within the first few minutes of mixing.

448



449

450 **Figure 12:** Heat flow and detail of the first 24 hours (a) and total heat (b) in isothermal calorimetry at
 451 20 °C during the first 7 days after mixing, normalized by the weight of VBA-800-6.

452

453 The leaching behavior of the VBA-800-6 was compared to BA sample, in order to identify the
 454 concentration of heavy metals in VBA and assure its use in construction materials. The leaching data
 455 are presented in Table 7.

456

457 Table 7: Leaching test results on raw BA and VBA samples (mg/kg).

| Element | Limit values for non-hazardous waste (EN 12457-4) | Limit values for inert waste (EN 12457-4) | Raw BA | VBA |
|------------|---|---|--------|---------|
| Antimony | 0.7 | 0.06 | 0.1987 | 0.0182 |
| Arsenic | 2 | 0.5 | 0.0541 | 0.0049 |
| Barium | 100 | 20 | 4.3125 | 0.0173 |
| Cadmium | 1 | 0.04 | 0.0333 | 0.0006 |
| Chromium | 10 | 0.5 | 0.8446 | 0.0053 |
| Copper | 50 | 2 | 6.5525 | 0.0383 |
| Lead | 10 | 0.2 | 1.8998 | 0.0153 |
| Molybdenum | 10 | 0.5 | 0.0691 | <0.0033 |
| Nickel | 10 | 0.4 | 0.4587 | <0.0014 |
| Zinc | 50 | 4 | 9.4422 | 0.0203 |

458

459 The amount of leached antimony, arsenic, chromium, copper, molybdenum, lead, nickel and zinc from
 460 BA do not comply with the limits for inert waste (EN 12457-7) (see Table 7), whereas the VBA is much

461 more resistant to leaching after vitrification and can even be classified as a non-hazardous waste. This
462 could be assigned to the volatilization of some heavy metals (e.g. arsenic, zinc, lead) during vitrification,
463 which is influenced by the complexing ligands and their volatilization tendency (Stabile et al., 2019),
464 and the immobilization of some elements (e.g. zinc, copper, nickel, chromium) in the glassy VBA
465 matrix.

466 The findings presented in this work shed light on the microwave processing of BA, forming the baseline
467 for a potentially viable upscaling process in a multimode furnace that allows a high throughput.

468

469 **Conclusions**

470 The feasibility and extent to which direct microwave BA vitrification can be realized as a waste
471 management technique was studied. The effect of microwave power and treatment time on the VBA
472 yield was assessed. A flash microwave process of the order of some seconds, was sufficient to initiate
473 BA feedstock vitrification with an energy requirement equal to 3300 kJ/kg. A higher energy input of
474 8600 kJ/kg resulted in a VBA yield of 86 wt%, the maximum conversion possible in the particular cold,
475 single-mode microwave cavity, without thermal insulation.

476 Electromagnetic field and thermal multiphysics' simulations complemented the experimental results,
477 revealing a power density driven heating mechanism, favored by a high power input and short
478 processing times. The non-thermal microwave-BA interactions generated localized microplasmas or
479 hot spots that prompted BA melting at high heating rates. The high volumetric BA bulk temperatures
480 achieved during processing, the intrinsic cold environment of the microwave cavity and the high silica
481 content of BA, promoted a fast enough cooling of the melt and the production of highly amorphous
482 VBA.

483 The leaching resistance of the VBA was successfully achieved from the microwave vitrification
484 process. The exothermal response of the VBA upon alkali-activation suggests its potential to be used
485 as precursor for alkali-activated materials, such as inorganic polymers.

486

487 **Acknowledgments**

488 This work was supported by the European Community's Horizon 2020 Programme under Grant
489 Agreement No. 721185 (MSCA-ETN NEW-MINE). This publication reflects only the authors' view,
490 exempting the Community from any liability. Project website: <http://new-mine.eu/>. G.Flesoura wishes
491 to thank Mohamed Adam, Adam Buttress and Gabriela Durán-Jiménez for the help and support during
492 the performed experiments at the University of Nottingham.

493

494 **References**

495 Alonso, S., Palomo, A., 2001. Calorimetric study of alkaline activation of calcium hydroxide-
496 metakaolin solid mixtures. *Cem. Concr. Res.* 31, 25–30. <https://doi.org/10.1016/S0008->

497 8846(00)00435-X

498 Blasenbauer, D., Huber, F., Lederer, J., Quina, M.J., Blanc-biscarat, D., Bogush, A., Bontempi, E.,
499 Blondeau, J., Maria, J., Dahlbo, H., Fagerqvist, J., Giro-paloma, J., Hjelmar, O., Hyks, J.,
500 Keaney, J., Lupsea-toader, M., Simon, F., Svecova, L., Joyce, C., Caollai, O., Orupöld, K., Paja,
501 T., Šyc, M., Ulvang, R., Vaajasaari, K., Caneghem, J. Van, Zomeren, A. Van, Vasarevic, S.,
502 Wégner, K., Fellner, J., 2020. Legal situation and current practice of waste incineration bottom
503 ash utilisation in Europe 102, 868–883. <https://doi.org/10.1016/j.wasman.2019.11.031>

504 Coelho, A.A., 2016. TOPAS-Academic, Version 6: Technical Reference 208.

505 European Commission-Environment, 2019. Landfill waste.
506 https://ec.europa.eu/environment/waste/landfill_index.htm (accessed 17 January 2020).

507 European Parliament and Council, 2018. Directive (EU) 2018/851 of the European Parliament and of
508 the council of 30 May 2018 amending Directive 2008/98/EC on waste. [https://eur-](https://eur-lex.europa.eu/legal-content/EN/TXT/PDF/?uri=CELEX:32018L0851&from=EN)
509 [lex.europa.eu/legal-content/EN/TXT/PDF/?uri=CELEX:32018L0851&from=EN](https://eur-lex.europa.eu/legal-content/EN/TXT/PDF/?uri=CELEX:32018L0851&from=EN) (accessed 17
510 January 2020)

511 Ferrera-Lorenzo, N., Fuente, E., Suárez-Ruiz, I., Ruiz, B., 2014. KOH activated carbon from
512 conventional and microwave heating system of a macroalgae waste from the Agar-Agar
513 industry. *Fuel Process. Technol.* 121, 25–31. <https://doi.org/10.1016/j.fuproc.2013.12.017>

514 Flesoura, G., Garcia-Banos, B., Catala-Civera, J.M., Vleugels, J., Pontikes, Y., 2019a. In-situ
515 measurements of high-temperature dielectric properties of municipal solid waste incinerator
516 bottom ash. *Ceram. Int.* 45, 18751-18759. <https://doi.org/10.1016/j.ceramint.2019.06.101>

517 Flesoura, G., Peys, A., Vleugels, J., Pontikes, Y., 2019b. Alkali activation of synthetic SiO₂-CaO-
518 FeOx-Al₂O₃-MgO glass, in: Malfiet, A., Peys, A., Di Maria, A. (Eds.), 6th International Slag
519 Valorisation Symposium. Procopia, Mechelen, Belgium, pp. 345–348.

520

521 Gao, X., Yu, Q.L., Lazaro, A., Brouwers, H.J.H., 2017. Investigation on a green olivine nano-silica
522 source based activator in alkali activated slag-fly ash blends: Reaction kinetics, gel structure and
523 carbon footprint. *Cem. Concr. Res.* 100, 129–139.

524 <https://doi.org/10.1016/j.cemconres.2017.06.007>

525 Hopwood, J., Hoskinson, A.R., Gregório, J., 2014. Microplasmas ignited and sustained by
526 microwaves. *Plasma Sources Sci. Technol.* 23. <https://doi.org/10.1088/0963-0252/23/6/064002>

527 Hotta, M., Hayashi, M., Nagata, K., 2010. Complex Permittivity and Permeability of 50, 1514–1516.

528 Huang, Q., Cai, X., Du, C., Chi, Y., Yan, J., 2014. Thermal plasma vitrification of MSWI fly ash
529 mixed with different biomass ashes. *IEEE Trans. Plasma Sci.* 42, 3549–3554.
530 <https://doi.org/10.1109/TPS.2014.2358626>

531 Joseph, A.M., Snellings, R., Van den Heede, P., Matthys, S., De Belie, N., 2018. The use of municipal
532 solidwaste incineration ash in various building materials: A Belgian point of view. *Materials*
533 (Basel). 11. <https://doi.org/10.3390/ma11010141>

534 Kappe, C.O., 2013. How to measure reaction temperature in microwave-heated transformations.
535 *Chem. Soc. Rev.* 42, 4977–4990. <https://doi.org/10.1039/c3cs00010a>

536 Kumar, S., Kumar, R., Mehrotra, S.P., 2010. Influence of granulated blast furnace slag on the
537 reaction, structure and properties of fly ash based geopolymer. *J. Mater. Sci.* 45, 607–615.
538 <https://doi.org/10.1007/s10853-009-3934-5>

539 Luukkonen, T., Abdollahnejad, Z., Yliniemi, J., Kinnunen, P., Illikainen, M., 2018. Comparison of
540 alkali and silica sources in one-part alkali-activated blast furnace slag mortar. *J. Clean. Prod.*
541 187, 171–179. <https://doi.org/10.1016/j.jclepro.2018.03.202>

542 Menéndez, J.A., Arenillas, A., Fidalgo, B., Fernández, Y., Zubizarreta, L., Calvo, E.G., Bermúdez,
543 J.M., 2010. Microwave heating processes involving carbon materials. *Fuel Process. Technol.* 91,
544 1–8. <https://doi.org/10.1016/j.fuproc.2009.08.021>

545 Menéndez, J.A., Juárez-Pérez, E.J., Ruisánchez, E., Bermúdez, J.M., Arenillas, A., 2011. Ball
546 lightning plasma and plasma arc formation during the microwave heating of carbons. *Carbon N.*
547 *Y.* 49, 346–349. <https://doi.org/10.1016/j.carbon.2010.09.010>

548 Mysen, B., Richet, M., 2005. *Silicate Glasses and Melts, Properties and Structure*, Elsevier S. ed.
549 Elsevier Science.

550 Norm EN 12457-4, 2002.

551 Onisei, S., Lesage, K., Blanpain, B., Pontikes, Y., 2015. *Early Age Microstructural Transformations*

552 of an Inorganic Polymer Made of Fayalite Slag. *J. Am. Ceram. Soc.* 98, 2269–2277.
553 <https://doi.org/10.1111/jace.13548>

554 Robinson, J.P., Kingman, S.W., Lester, E.H., Yi, C., 2012. Microwave remediation of hydrocarbon-
555 contaminated soils - Scale-up using batch reactors. *Sep. Purif. Technol.* 96, 12–19.
556 <https://doi.org/10.1016/j.seppur.2012.05.020>

557 Rosenholtz, J.L., Smith, D.T., 1936. The Dielectric Constant of Mineral Powders. *Am. Mineral.* 21,
558 115–120.

559 Shang, H., Snape, C.E., Kingman, S.W., Robinson, J.P., 2006. Microwave treatment of oil-
560 contaminated North Sea drill cuttings in a high power multimode cavity. *Sep. Purif. Technol.* 49,
561 84–90. <https://doi.org/10.1016/j.seppur.2005.08.012>

562 Slood, H.A. Van Der, Kosson, D.S., Hjelmar, O., 2001. Characteristics , treatment and utilization of
563 residues from municipal waste incineration. *Waste Manag.* 21, 753–765.
564 [https://doi.org/https://doi.org/10.1016/S0956-053X\(01\)00009-5](https://doi.org/https://doi.org/10.1016/S0956-053X(01)00009-5)

565 Stabile, P., Bello, M., Petrelli, M., Paris, E., Carroll, M.R., 2019. Vitrification treatment of municipal
566 solid waste bottom ash. *Waste Manag.* 95, 250–258.
567 <https://doi.org/10.1016/j.wasman.2019.06.021>

568 Wei, Y., Shimaoka, T., Saffarzadeh, A., Takahashi, F., 2011. Alteration of municipal solid waste
569 incineration bottom ash focusing on the evolution of iron-rich constituents. *Waste Manag.* 31,
570 1992–2000. <https://doi.org/10.1016/j.wasman.2011.04.021>

571 Woollacott, L.C., Howat, D.D., Jochens, P.R., 1975. The viscosities and electrical conductivities of
572 slags associated with the production of high-carbon ferromanganese alloys, in: Infacon (Ed.),
573 The First International Ferroalloys Congress. Johannesburg, South Africa, pp. 227–232.

574 Xin-Hui, D., Srinivasakannan, C., Jin-Hui, P., Li-Bo, Z., Zheng-Yong, Z., 2011. Preparation of
575 activated carbon from *Jatropha* hull with microwave heating: Optimization using response
576 surface methodology. *Fuel Process. Technol.* 92, 394–400.
577 <https://doi.org/10.1016/j.fuproc.2010.09.033>

578 Yuan, X., Qing, Q., Zhang, S., Lu, X., 2017. Vitrification of Radioactive Contaminated Soil by Means
579 of Microwave Energy, in: AIP Conference Proceedings. American Institute of Physics (United

580 States). <https://doi.org/10.1063/1.4977304>

581 Zhang, S., Ding, Y., Lu, X., Mao, X., Song, M., 2016. Rapid and efficient disposal of radioactive

582 contaminated soil using microwave sintering method. Mater. Lett. 175, 165–168.

583 <https://doi.org/10.1016/j.matlet.2016.04.018>

584

585

586

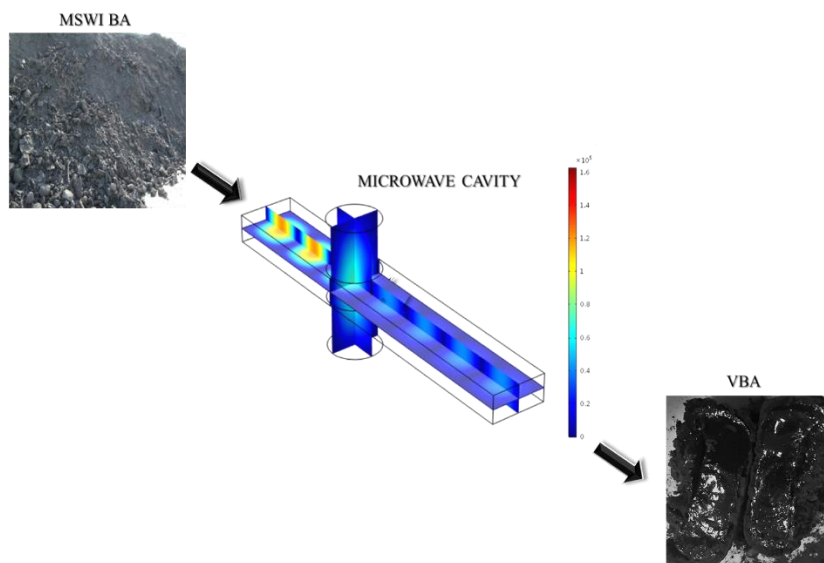
587

588

589 Graphical Abstract

590

- 591 • Realization of flash microwave vitrification of BA with 3300 kJ/kg energy input
- 592 • Energy density driven heating mechanism of BA favored by high power input and short
- 593 processing time
- 594 • Microplasmas prompting BA melting at high heating rates
- 595 • Promising use of VBA as a precursor for alkali-activated materials



596